NANO LETTERS

pubs.acs.org/NanoLett

Letter

Intelligent Phase Contrast Meta-Microscope System

Cheng Hung Chu, Yu-Hsin Chia, Hung-Chuan Hsu, Sunil Vyas, Chen-Ming Tsai, Takeshi Yamaguchi, Takuo Tanaka, Huei-Wen Chen, Yuan Luo,* Pan-Chyr Yang,* and Din Ping Tsai*

Cite This: *Nano Lett.* 2023, 23, 11630−11637

Read Online

ACCESS | Metrics & More | Article Recommendations | Supporting Information

ABSTRACT: Phase contrast imaging techniques enable the visualization of disparities in the refractive index among various materials. However, these techniques usually come with a cost: the need for bulky, inflexible, and complicated configurations. Here, we propose and experimentally demonstrate an ultracompact meta-microscope, a novel imaging platform designed to accomplish both optical and digital phase contrast imaging. The optical phase contrast imaging system is composed of a pair of metalenses and an intermediate spiral phase metasurface located at the Fourier plane. The performance of the system in generating edge-enhanced images is validated by imaging a variety of human cells, including lung cell lines BEAS-2B, CLY1, and H1299 and other types. Additionally, we integrate the ResNet deep learning model into the meta-microscope to transform bright-field images into edge-enhanced images with high contrast accuracy. This technology promises to aid in the development of innovative miniature optical systems for biomedical and clinical applications.

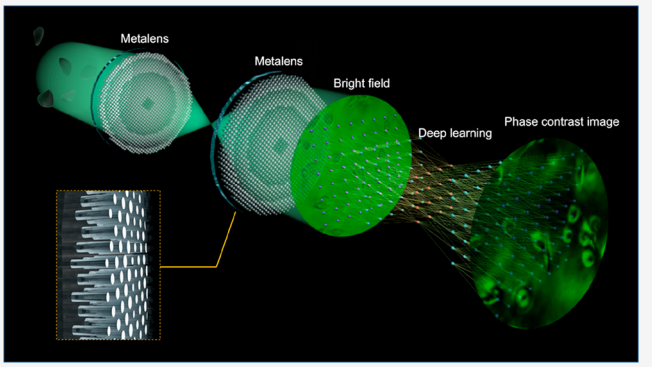

KEYWORDS: *metasurface, phase contrast imaging, edge detection, deep learning*

Bright-field microscopy has been a bedrock in biological applications, lighting the path to the structural exploration of cells. Despite its significance, it falls short in imaging limited contrast biological samples. Traditional attempts to improve this, such as staining, carry their own challenges, including complex preparation processes and potentially harmful effects on living samples. Many approaches have been devised to make weakly scattered specimens visible such as dark-field and phase contrast microscopies. In particular, phase contrast microscopy has played a pivotal role in shaping the landscape of contemporary biology and medicine, offering unprecedented insights into the cellular world. Phase contrast microscopy, invented by Frits Zernike, enables the visualization of transparent cells by converting their phase variations into visible intensity using a specialized phase plate with a thickness gradient and a condenser annulus stop.[1−3] Another well-known phase contrast technology is differential interference contrast (DIC) microscopy using paired Wollaston prisms to produce the polarization-based wavefront shearing interference effect.[4,5] However, the implementation of multiple cascaded phase contrast elements makes these systems complicated. In contrast, spiral phase contrast microscopy offers a simpler configuration while also providing an edge contrast enhancement effect for both amplitude and phase samples.[6−9] The spiral phase plate, placed at the Fourier plane of the 4-*f* microscope system, functions as a radial Hilbert transform spatial filter that offers valuable image processing capabilities.[10,11] Generally, the spiral phase mask is created by a phase-only liquid-crystal spatial light modulator (SLM), s-plate, or q-plate. Despite their utility in this regard, they usually suffer from low resolution, high cost, and bulkiness, thereby restricting their applicability in compact optical systems.

A nanophotonic metasurface as a transformative technology has swept over the optical world in the past decade due to its provocative performance and high applicability for conventional optical systems.[12−22] Metasurfaces are constructed from artificial optical nanoresonators that can exert precise control over the intensity and phase of electromagnetic waves, thereby enabling a wide range of on-demand functions. Metalenses, a subset of metasurfaces specifically designed for focusing, have already been intensively utilized in a variety of biomedical imaging fields, such as endomicroscopy, light sheet fluorescence microscopy, etc.,[23−29] allowing device designs more compact than those of their conventional counterparts. Recently, computing metasurfaces have been proposed, offering optically mathematical operations like spatial first-order and second-order differentiation and filtering, which are essential for image processing and analysis.[30−38] However,

Received: September 11, 2023
Revised: November 25, 2023
Accepted: November 27, 2023
Published: December 1, 2023

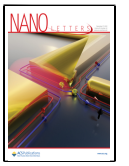

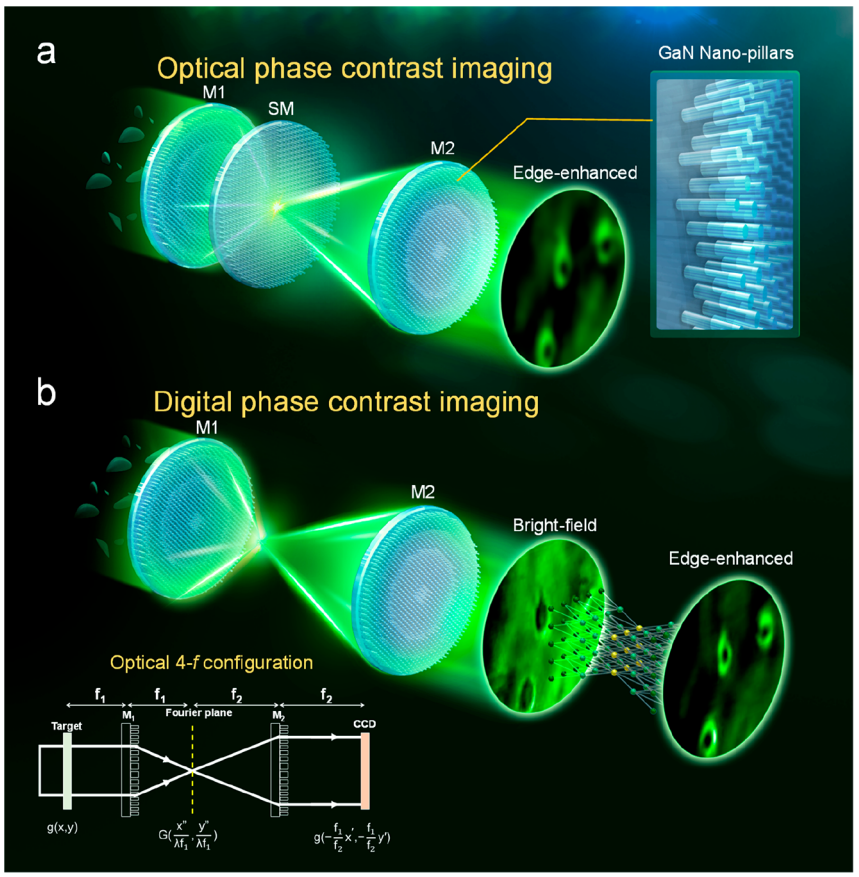

Figure 1. Schematic diagram of the all-metasurface. (a) Optical phase contrast imaging systems. (b) Digital phase contrast imaging systems based on a deep learning algorithm. The inset shows the schematic diagram of the optical 4-*f* imaging configuration. Abbreviations: M1, metalens 1; M2, metalens 2; SM, spiral phase metasurface.

most of the previous works substitute only a few optical elements with metasurfaces, resulting in the conventional optical components still dominating the performance of the system. For example, while the spiral metalens based on the geometric method design proposed by Kim et al. shows promising results in isotropic edge-enhanced imaging, it still relies on the support of conventional circular polarizers, an objective, and a tube lens.[33]

In recent years, deep neural network-based (DNN) approaches have shown their remarkable ability to assist with a wide range of biomedical imaging tasks, such as object detection, cell segmentation, and image-to-image translations.[39−42] Via combination of optics and deep learning (DL) imaging algorithms, it is possible to enhance the quality and accuracy of images while simultaneously reducing the system complexity of optical microscopes and minimizing processing times.[43−48] Moreover, DNNs have recently been used to solve the challenges of metasurfaces, covering areas from fundamental unit cell design to a variety of imaging enhancements such as chromatic aberration correction, noise suppression, and contrast loss compensation.[49−55] The remarkable results of DNNs suggest that these approaches may become increasingly common in the development of innovative imaging solutions in the years to come.

Here we propose and experimentally demonstrate an ultracompact meta-microscope as a platform, without any conventional optical element support, to achieve both digital and optical phase contrast imaging. First, the imaging capability of the meta-microscope is validated by using various samples. Then, the spiral phase metasurface, as the radial Hilbert spatial filter, is used to suppress low-frequency and amplify high-frequency components to obtain edge-enhanced images. In addition, we present the use of a DL algorithm to convert the bright-field images to edge-enhanced images. To the best of our knowledge, this is the first report on the entire-metasurface 4-*f* optical configuration for phase contrast imaging. The hardware and computational innovations introduced by our technology may have significant practical benefits in various microscopies for clinical purposes, especially in situations in which the size of the system plays a crucial role.

The principles of optical and digital phase contrast imaging with a meta-microscope are illustrated in Figure 1. The meta-microscope is based on an optical 4-*f* imaging configuration that consists of two metalenses, separated by a distance related to their focal lengths $(f_1 + f_2)$ with a Fourier plane between them, as shown in the inset for details. The first metalens focuses the incoming light onto the Fourier plane, where it is converted into its spatial frequency components by a Fourier transform. The spatial frequency filters can be placed at the Fourier plane, which enables analysis, modulation, or extraction of the image in terms of its frequency components to reveal significant details about its structure and content. For example, low spatial frequencies are associated with regions of gradual change, such as smooth surfaces, whereas high spatial frequencies are associated with areas of rapid change in intensity such as edges. In addition, the magnification (M) of an output image is determined by the ratio of the focal lengths of the metalenses $(M = f_2/f_1)$. The second metalens is used to

https://doi.org/10.1021/acs.nanolett.3c03484
Nano Lett. 2023, 23, 11630−11637

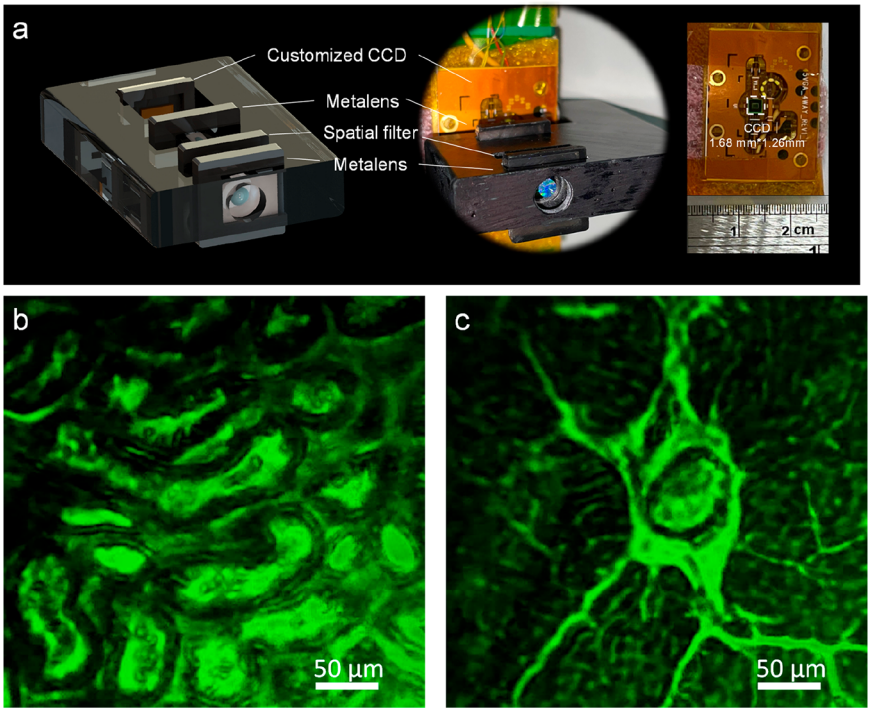

Figure 2. (a) Prototype of the meta-microscope. (b) Bright-field image of epithelial cells. (c) Bright-field image of pancreas islets cells.

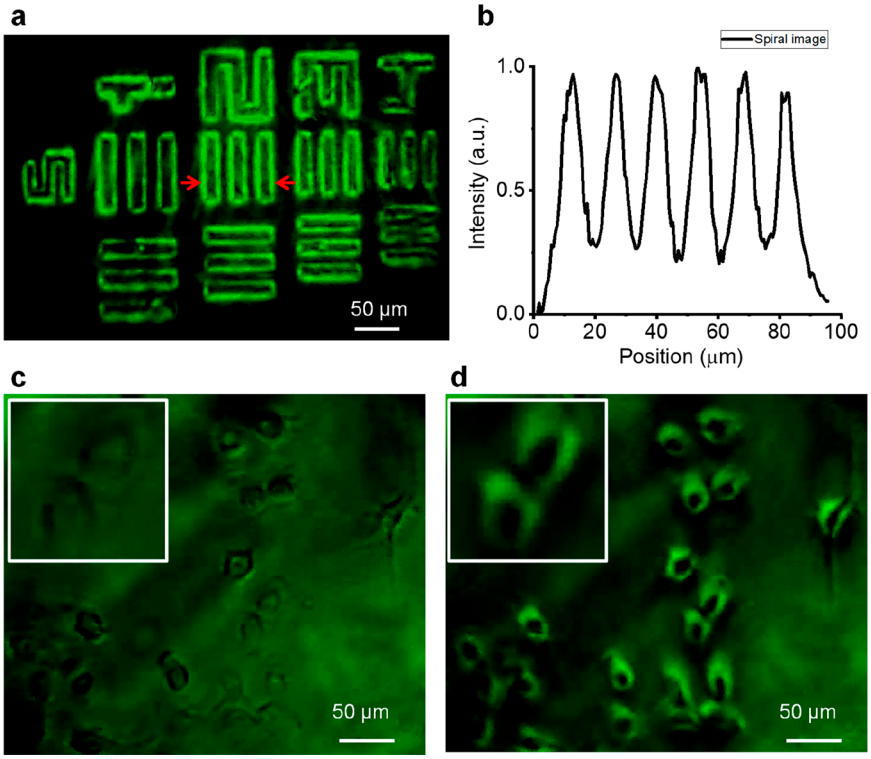

Figure 3. (a) Edge-enhanced image of the 1951 USAF resolution test chart obtained by a meta-microscope with a spiral phase metasurface. (b) Normalized intensity distribution along the red arrows marked in panel a. (c) Bright-field image of lung cancer H1299 cells. (d) Corresponding edge-enhanced image of panel c.

perform an inverse Fourier transform to generate the output image. In this work, we use the spiral phase metasurface to provide the function of spatial differentiation for realizing edge enhancement of the image shown in Figure 1a. On the contrary, in digital phase contrast imaging, a bright-field image obtained from the meta-microscope can be converted into an edge-enhanced image by using a well-trained DL neural network model shown in Figure 1b.

Figure 2a shows the assembled meta-microscope prototype, where the supporting housing is made by three-dimensional printing. The customized CCD (384 pixels × 288 pixels; pixel size, 1.75 μm × 1.75 μm) is used for imaging. The phase

https://doi.org/10.1021/acs.nanolett.3c03484
Nano Lett. 2023, 23, 11630−11637

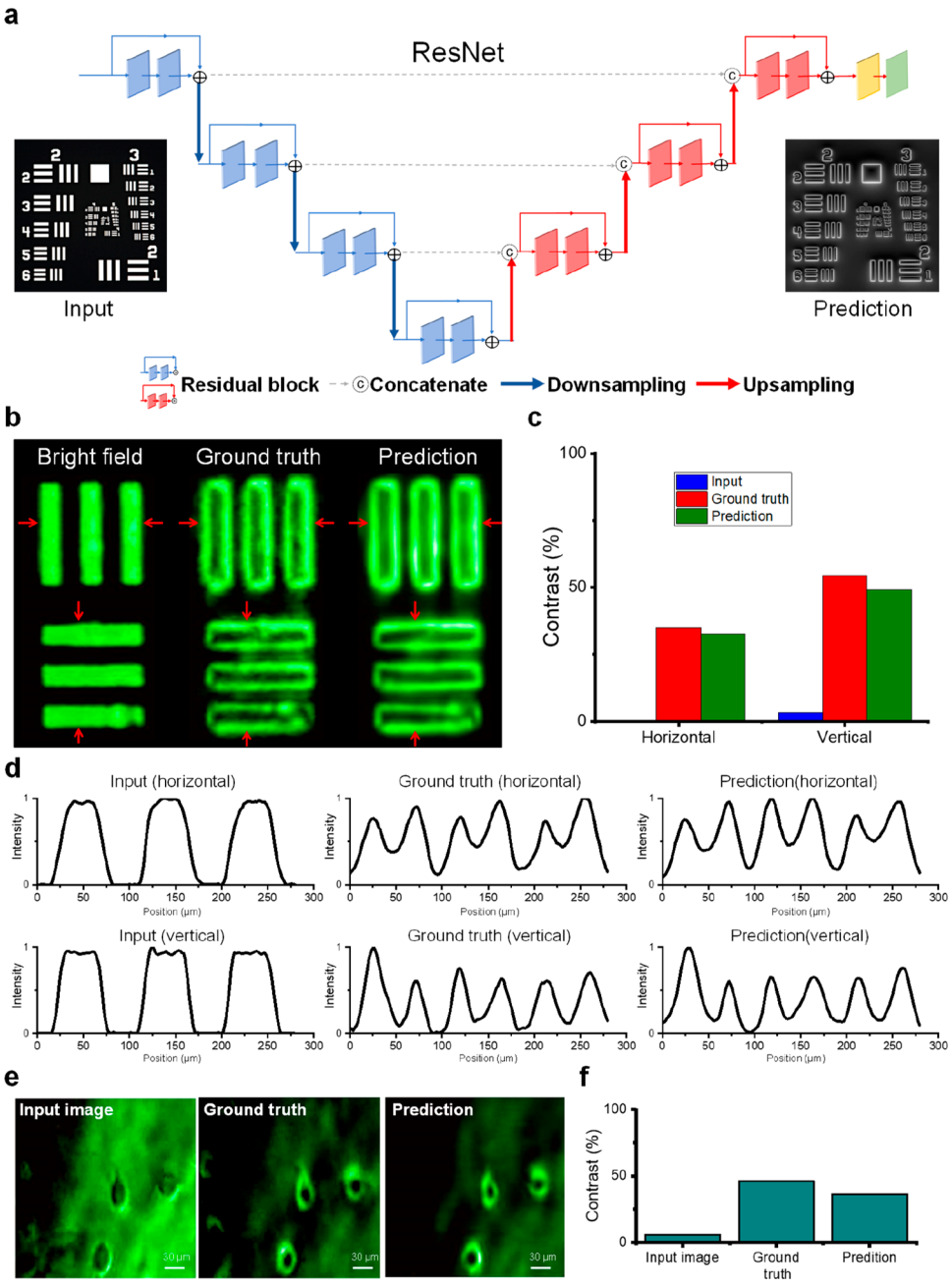

Figure 4. (a) Architecture of the ResNet model for converting a bright-field image into an edge contrast enhancement image. (b) Bright-field image (input), edge-enhanced image (ground truth), and DL-based edge-enhanced image (prediction) of group 5 element 1 of the 1951 USAF resolution chart. (c) Average edge contrast plot along the horizontal and vertical directions. (d) Corresponding horizontal and vertical direction profiles in panel b. (e) Bright-field image (input), edge-enhanced image (ground truth), and DL-based edge-enhanced images (prediction) of H1299 cells. (f) Average edge contrast plot of H1299 cells in panel e.

distribution of metalenses is designed by the following equation:[56]

$$\varphi(r) = \frac{2\pi}{\lambda}(f - \sqrt{f^2 + r^2}),$$

where λ is the working wavelength, f is the focal length, and r is the polar radius of the metalens. Meta-atoms, varying-diameter gallium nitride (GaN) cylindrical nanopillars on the Al_2O_3 substrate, are designed by using the commercial full-wave electromagnetic software Computer Simulation Technology (CST) Microwave Studio. GaN and Al_2O_3 have a transparency window for the entire visible light range. The height of GaN nanopillars is 850 nm. The periodic boundary conditions with a pitch of 280 nm are applied along the x- and y-axes, and the opening model along the propagation direction (z-axis). The cylindrical nanopillars are insensitive to polarization (linear and circular in the x−y plane). A linearly polarized electromagnetic plane wave is used as a normally incident excitation source. At the operation wavelength of 532 nm, GaN has the real part of a refractive index of 2.4, which is high enough to have significant interaction with light to form waveguide-like resonant modes, and its imaginary part is negligible.[57] The phase shifts and transmissions of GaN cylindrical nanopillars with different diameters are shown in Figure S1. The full 2π

https://doi.org/10.1021/acs.nanolett.3c03484
Nano Lett. 2023, 23, 11630−11637

phase modulation can be realized by varying the diameter from 100 to 185 nm. The average efficiency of meta-atoms is ∼88%. With a 2 mm diameter, the focal lengths of two metalenses are 5 and 10 mm, and the corresponding numerical apertures are 0.26 and 0.13, respectively. Therefore, the axial size of the meta-microscope with 2× magnification is ∼3 cm, which is much smaller than those of traditional microscopes. The metalenses are fabricated by using standard electron beam lithography and several hard mask transfers by using etching processes. More details of the fabrication processes and characteristics of the metalens, including the scanning electron microscope (SEM) image and measured intensity profile of the focusing beam, can be found in Methods and Figures S2 and S3. To demonstrate the imaging ability of our meta-microscope for biospecimens, the representative bright-field images of stained epithelium cells and pancreas islets cells are shown in panels b and c, respectively, of Figure 2. The imaging setup is shown in Figure S4a. The cells are illuminated by a plane wave produced by a commercially available laser-driven light source (LDLS), with a bandwidth filter at a center wavelength of 532 nm, which can provide spatially partial coherent illumination. The resolution of the system is validated by using the standard 1951 USAF resolution test chart. The lateral resolution of this system can be achieved at ∼2 μm, as shown in Figure S5.

Figure 3a shows the edge-enhanced image of group 5 of the 1951 USAF resolution test chart formed by using the optical phase contrast imaging system. The imaging setup is shown in Figure S4b. The GaN metasurface-based spiral phase plate is placed in the back focal plane of the first metalens, the Fourier plane of the meta-microscope system. The metasurface-based design can provide more accurate phase control and higher resolution in comparison to those of conventional phase plates. The diameter of the spiral phase metasurface is 0.8 mm. Spiral phase $\varphi(r, \theta)$ is written as

$$\varphi(r, \theta) = \exp(im\theta)$$

where r and θ are the radial distance and azimuthal angle, respectively, and m is the topological charge. The phase distribution with a topological charge of 1 is shown in Figure S6a, where the phases between 0 and 2π are represented by the grayscale values. Through the phase modulation of the spiral phase plate, phase variations are transformed into intensity variations, resulting in edge enhancement (a more detailed mathematical explanation of the convolution between the input image and radial Hilbert transform can be found in Figure S6). The discontinuities in the image of the pattern can be attributed to the contaminants on the resolution test chart, which can be observed in Figure S5a. The normalized intensity distribution between the red arrows is shown in Figure 3b. The intensities of the six peaks from the edges are consistent. The average edge contrast is ∼58%, which is much higher than that of the bright-field image, with an average contrast of ∼3%. The edge contrast is defined as $C = (I_{max} - I_{min})/(I_{max} + I_{min})$, where I_{max} and I_{min} are the maximum and minimum intensities, respectively, of the edges. Next, to show the capability of our system in terms of the edge enhancement of phase objects, we employ label-free cells that have minimal changes in both their refractive index and thickness. Panels c and d of Figure 3 show both bright-field and edge-enhanced images of human lung cancer H1299 cells in phosphate-buffered saline (PBS). The bright-field image of H1299 cells has poor contrast due to strong background with low-frequency components, while the edge-enhanced cell image is shown in Figure 3d because the spiral phase metasurface isotropically suppresses low-frequency and amplifies high-frequency components.

The convolutional neural network ResNet-based architecture, an improved alternative to the conventional CNN model, has been extensively utilized in image transformation for biomedical imaging. It is faster and more flexible in terms of delivering fine features at varying sizes, especially in situations in which a small training data set is available. Here, the ResNet model employed for digital phase contrast imaging is shown in Figure 4a. A detailed description of the ResNet model and its training approach can be found in Methods. Figure 4b shows the results of the DL-based edge-enhanced images in the USAF chart. The bright-field images are input; phase contrast images obtained from the meta-microscope are ground truth, and the predicted edge-enhanced images are transferred by the well-trained ResNet model. Here, we use edge contrast values as the quantitative index to assess the performance of well-trained models. Panels c and d of Figure 4 show the edge contrast values along both vertical and horizontal directions and the corresponding intensity profiles. The edge contrasts of vertical and horizontal profiles obtained from the optical phase contrast imaging (ground truth) are 54% and 35%, respectively, and the corresponding results predicted by the well-trained ResNet model (prediction) are 49% and 33%, respectively. As expected, they are well-matched with each other. The vertical and horizontal results are inconsistent because the incident light source is not uniform. The predicted image of patterns with wider line widths (group 4 element 1) maintains a similar edge contrast level as shown in Figure S7. Next, we convert bright-field images of human lung cancer H1299 cells, which are absent from the training data set, into edge-enhanced images by using the trained model. The prediction of different cells shown in Figure 4e provides edge enhancement characteristics similar to the result of the optical phase contrast imaging. Their corresponding average edge contrasts of cells in Figure 4f also show high contrast consistency between DL-based and metasurface-based edge-enhanced images. Furthermore, the ability of our model can be quantitatively assessed using an absolute error map, wherein one is the difference between the input images and the ground truth and another is the difference between the ground truth and the predicted images. The resulting images, particularly those of H1299 and thyroid cells, display minimal error, affirming that the ResNet model's predictions closely align with the ground truth as shown in Figure S8.

CONCLUSION

In summary, we propose the ultracompact meta-microscope for optical and digital phase contrast imaging to obtain isotropic edge-enhanced images of the standard resolution chart, as well as various types of human cells. The meta-microscope in the 4-f imaging configuration is flexible and can be paired with different spatial frequency filters to extend its capabilities. Optical spiral phase contrast imaging with a meta-microscope significantly improved the edge contrast to ∼58% compared to the bright-field image contrast of ∼3%. Deep learning-based digital phase contrast imaging effectively creates isotropic edge-enhanced human cell images, paralleling the results of optical phase contrast imaging. The outcome from both techniques is not about superiority but flexibility, as both deliver high-quality results in different scenarios to meet specific needs. Considering the compact size and flexibility of

https://doi.org/10.1021/acs.nanolett.3c03484
Nano Lett. 2023, 23, 11630−11637

our meta-microscope, it can be integrated into miniaturized biomedical imaging systems, especially in space-constrained environments such as portable stain-free cell imaging systems. Furthermore, its suitability can be extended to invasive medical procedures, such as those involving flexible ureteroscopes and capsule endoscopy cameras, due to the nontoxic, non-inflammatory, and hypoallergenic nature of its constituent materials, GaN and Al_2O_3. These materials are also highly chemically and mechanically stable, significantly reducing the potential risks to patients. We believe that optical and digital meta-microscope imaging systems can steer the biomedical field toward novel, groundbreaking directions.

METHODS

Fabrication of the GaN Metalens. The fabrication of GaN nanopillars relies on the typical electron beam lithography and reactive ion etching process (RIE), as shown in Figure S2. The 850 nm thick GaN and 200 nm thick SiO_2 layers are sequentially deposited on the 450 μm thick c-plane Al_2O_3 substrate by using metal−organic chemical vapor deposition (MOCVD) and an electron-gun evaporator, respectively. PMMA A4, the electron beam resist, is coated onto the substrate by spin coaters. The exposure procedure is carried out with electron beam lithography equipment (Elionix ELS-HS50) with a beam current of 1 nA and an accelerating voltage of 50 kV. The exposed substrate is developed by using the developer solution (1:3 MIBK:IPA) followed by deposition of a 40 nm chromium layer by using an electron-gun evaporator to function as the hard mask layer. Two-step reactive ion etching (RIE) is then performed using CF_4 to etch SiO_2 and a mixed gas composed of Cl_2 and Ar to etch GaN. Finally, the metalens consisting of GaN nanopillars on a sapphire substrate is obtained by removing the SiO_2 using a buffered oxide etch (BOE) solution.

ResNet Model. The ResNet model is a symmetric structure composed of an encoding branch and a decoding branch. The input layer consists of the bright-field images obtained by our meta-microscope. Three 3 × 3 convolutions, with stride 2 and padding 1 followed by an activation function leaky ReLU with slope 0.01 for the feature extraction with a 2 × 2 maximum, are applied along the encoding branch for downsampling. The number of feature channels (or depth) is increased to twice at each downsampling. Inversely, the expansive path consists of 2 × 2 up-convolution and two 3 × 3 convolutions followed by the leaky ReLU with slope 0.01, where the size of the image increases and the depth decreases. Each feature vector has 64 components, and at the last layer, a 1 × 1 convolution is utilized to transfer those components to the target number of classes. The skip connections, the bypassing of convolutional layer blocks, are used to relay the feature information from a low level to a high level in the up-sampling process. The network consists of a total of 22 convolutional layers. The ground truth and input training images are obtained via the meta-microscope system, with and without the spiral phase metasurface. The bright-field and corresponding edge-enhanced images of five different types of cells, including BEAS-2B, CLY1, H1299, thyroid, and uterus cells, are used for the training shown in Figure S9. Data augmentation is utilized for horizontal flipping and vertical flipping for 30% of the total data set (1064 images) to increase the size of the data set.[58] The data set is divided into training, validation, and test data sets with a ratio of 8:1:1 to minimize overfitting.[59] In the evaluation procedure, the mean square error (MSE) as the loss function and the Adam optimization technique as the optimizer are used.[60,61] The training data sets are used to update the weights in each kernel during the training process to minimize the loss value. The weights of the model are stored at each epoch when the validation loss is at its minimum. Once the training process is finished, the performance of the model is evaluated using the testing data sets. The learning rate and the number of epochs are set as 1×10^{-3} and 1000, respectively. Our model is trained and tested using Pytorch on a workstation equipped with dual NVIDIA RTX A5000 GPUs (24 GB VRAM) and an Intel Xeon Silver 4210R 2.4 GHz CPU (two cores).

ASSOCIATED CONTENT

Data Availability Statement

The data that support the plots within this paper and other findings of this study are available from the corresponding author upon reasonable request.

Supporting Information

The Supporting Information is available free of charge at https://pubs.acs.org/doi/10.1021/acs.nanolett.3c03484.

Details of the GaN unit cell design, nanofabrication processes of metasurfaces, beam profile measurement, configuration of spiral phase contrast microscopy with a meta-microscope, bright-field imaging of the resolution chart obtained with the meta-microscope, convolution with a spiral phase plate, prediction result of the resolution chart, absolute error map, different types of cells for model training, encoder architecture of the ResNet model, and decoder architecture of the ResNet model (PDF)

AUTHOR INFORMATION

Corresponding Authors

Yuan Luo − *YongLin Institute of Health, National Taiwan University, Taipei 10672, Taiwan; Institute of Medical Device and Imaging and Department of Biomedical Engineering, National Taiwan University, Taipei 10051, Taiwan; Program for Precision Health and Intelligent Medicine, National Taiwan University, Taipei 106319, Taiwan, R.O.C.;* orcid.org/0000-0001-9776-7897; Email: yuanluo@ntu.edu.tw

Pan-Chyr Yang − *YongLin Institute of Health, National Taiwan University, Taipei 10672, Taiwan; Program for Precision Health and Intelligent Medicine, National Taiwan University, Taipei 106319, Taiwan, R.O.C.; Department of Internal Medicine, National Taiwan University Hospital, National Taiwan University, Taipei 10002, Taiwan; Institute of Biomedical Sciences, Academia Sinica, Taipei 11529, Taiwan*; Email: pcyang@ntu.edu.tw

Din Ping Tsai − *Department of Electrical Engineering and Centre for Biosystems, Neuroscience, and Nanotechnology, City University of Hong Kong, Kowloon 999077, Hong Kong; The State Key Laboratory of Terahertz and Millimeter Waves, City University of Hong Kong, Kowloon 99907, Hong Kong;* orcid.org/0000-0002-0883-9906; Email: dptsai@cityu.edu.hk

Authors

Cheng Hung Chu − *YongLin Institute of Health, National Taiwan University, Taipei 10672, Taiwan;* orcid.org/0000-0002-8749-3930

https://doi.org/10.1021/acs.nanolett.3c03484
Nano Lett. 2023, 23, 11630−11637

Yu-Hsin Chia − *Institute of Medical Device and Imaging and Department of Biomedical Engineering, National Taiwan University, Taipei 10051, Taiwan*
Hung-Chuan Hsu − *Department of Mechanical Engineering, National Taiwan University, Taipei 10617, Taiwan*
Sunil Vyas − *Institute of Medical Device and Imaging, National Taiwan University, Taipei 10051, Taiwan*
Chen-Ming Tsai − *Institute of Medical Device and Imaging, National Taiwan University, Taipei 10051, Taiwan*
Takeshi Yamaguchi − *Innovative Photon Manipulation Research Team, RIKEN Center for Advanced Photonics, Saitama 351-0198, Japan;* orcid.org/0000-0002-7085-455X
Takuo Tanaka − *Innovative Photon Manipulation Research Team, RIKEN Center for Advanced Photonics, Saitama 351-0198, Japan;* orcid.org/0000-0001-5714-5401
Huei-Wen Chen − *Graduate Institute of Toxicology, College of Medicine, National Taiwan University, Taipei 100, Taiwan; Genome and Systems Biology Degree Program, National Taiwan University and Academia Sinica, Taipei 100, Taiwan*

Complete contact information is available at: https://pubs.acs.org/10.1021/acs.nanolett.3c03484

Author Contributions

C.H.C., Y.L., and D.P.T. conceived the principle and method of experiments and the design of the metasurfaces. C.H.C., T.Y., and T.T. fabricated the metasurfaces. C.H.C., Y.-H.C., H.-C.H., S.V., and C.-M.T. performed the optical measurement and data analysis. H.-W.C. and P.-C.Y. provided the human cell lines and contributed to human cell line experiments. Y.L., P.-C.Y., and D.P.T. organized the project and experiments. All authors discussed and analyzed the results and prepared the manuscripts.

Notes

The authors declare no competing financial interest.

■ ACKNOWLEDGMENTS

The authors acknowledge financial support from the Ministry of Science and Technology, Taiwan (Grants MOST-106-2221-E-002-157-MY3 and MOST-108-2221-E-002-168-MY4), National Taiwan University (Grants NTU-107L7728, NTU-107L7807, and NTU-YIH-08HZT49001), the University Grants Committee/Research Grants Council of the Hong Kong Special Administrative Region, China (Project AoE/P-502/20, CRF Projects C1015-21E and C5031-22G, and GRF Projects CityU15303521, CityU11305223, CityU11310522, and CityU11300123), the City University of Hong Kong (Projects 9380131 and 7005867), and JST CREST (Grant JPMJCR1904).

■ REFERENCES

(1) Zernike, F. Phase contrast, a new method for the microscopic observation of transparent objects. *Physica* **1942**, *9*, 686−698.
(2) Liang, R.; Erwin, J. K.; Mansuripur, M. Variation on Zernike's phase-contrast microscope. *Appl. Opt.* **2000**, *39*, 2152−2158.
(3) Gao, P.; Yao, B.; Harder, I.; Lindlein, N.; Torcal-Milla, F. J. Phase-shifting Zernike phase contrast microscopy for quantitative phase measurement. *Opt. Lett.* **2011**, *36*, 4305−4307.
(4) Franz, G.; Kross, J. Generation of two-dimensional surface profiles from differential interference contrast (DIC)—images. *Optik* **2001**, *112*, 363−367.
(5) Arnison, M. R.; Larkin, K. G.; Sheppard, C. J.; Smith, N. I.; Cogswell, C. J. Linear phase imaging using differential interference contrast microscopy. *J. Microsc.* **2004**, *214*, 7−12.
(6) Cheng, S.; et al. Partially coherent spiral phase contrast imaging with a 3D-like effect. *Appl. Phys. Express* **2022**, *15*, No. 092004.
(7) Fürhapter, S.; Jesacher, A.; Bernet, S.; Ritsch-Marte, M. Spiral phase contrast imaging in microscopy. *Opt. Express* **2005**, *13*, 689−694.
(8) Maurer, C.; Jesacher, A.; Fürhapter, S.; Bernet, S.; Ritsch-Marte, M. Upgrading a microscope with a spiral phase plate. *J. Microsc.* **2008**, *230*, 134−142.
(9) Situ, G.; Warber, M.; Pedrini, G.; Osten, W. Phase contrast enhancement in microscopy using spiral phase filtering. *Opt. Commun.* **2010**, *283*, 1273−1277.
(10) Davis, J. A.; McNamara, D. E.; Cottrell, D. M.; Campos, J. Image processing with the radial Hilbert transform: theory and experiments. *Opt. Lett.* **2000**, *25*, 99−101.
(11) Guo, C.-S.; Han, Y.-J.; Xu, J.-B.; Ding, J. Radial Hilbert transform with Laguerre-Gaussian spatial filters. *Opt. Lett.* **2006**, *31*, 1394−1396.
(12) Yu, N.; et al. Light propagation with phase discontinuities: generalized laws of reflection and refraction. *science* **2011**, *334*, 333−337.
(13) Sun, S.; et al. High-efficiency broadband anomalous reflection by gradient meta-surfaces. *Nano Lett.* **2012**, *12*, 6223−6229.
(14) Lin, D.; Fan, P.; Hasman, E.; Brongersma, M. L. Dielectric gradient metasurface optical elements. *science* **2014**, *345*, 298−302.
(15) Zheng, G.; et al. Metasurface holograms reaching 80% efficiency. *Nat. Nanotechnol.* **2015**, *10*, 308−312.
(16) Chu, C. H.; et al. Active dielectric metasurface based on phase-change medium. *Laser Photonics Rev.* **2016**, *10*, 986−994.
(17) Hsiao, H. H.; Chu, C. H.; Tsai, D. P. Fundamentals and applications of metasurfaces. *Small Methods* **2017**, *1*, 1600064.
(18) Tittl, A.; et al. Imaging-based molecular barcoding with pixelated dielectric metasurfaces. *Science* **2018**, *360*, 1105−1109.
(19) Yesilkoy, F.; et al. Ultrasensitive hyperspectral imaging and biodetection enabled by dielectric metasurfaces. *Nat. Photonics* **2019**, *13*, 390−396.
(20) Luo, Y.; et al. Metasurface-Based Abrupt Autofocusing Beam for Biomedical Applications. *Small Methods* **2022**, *6*, 2101228.
(21) Zhou, J.; et al. Optical edge detection based on high-efficiency dielectric metasurface. *Proceedings of the National Academy of Sciences* **2019**, *116*, 11137−11140.
(22) Zhang, X.; et al. Multifocal Plane Display Based on Dual Polarity Stereoscopic Metasurface. *Adv. Funct. Mater.* **2022**, *32*, 2209460.
(23) Arbabi, A.; Faraon, A. Advances in optical metalenses. *Nat. Photonics* **2023**, *17*, 16−25.
(24) Arbabi, E.; et al. MEMS-tunable dielectric metasurface lens. *Nat. Commun.* **2018**, *9*, 812.
(25) Khorasaninejad, M.; et al. Metalenses at visible wavelengths: Diffraction-limited focusing and subwavelength resolution imaging. *Science* **2016**, *352*, 1190−1194.
(26) Li, L.; et al. Metalens-array−based high-dimensional and multiphoton quantum source. *Science* **2020**, *368*, 1487−1490.
(27) Lin, R. J.; et al. Achromatic metalens array for full-colour light-field imaging. *Nat. Nanotechnol.* **2019**, *14*, 227−231.
(28) Xu, B.; et al. Metalens-integrated compact imaging devices for wide-field microscopy. *Adv. Photonics* **2020**, *2*, 066004−066004.
(29) Luo, Y.; et al. Varifocal metalens for optical sectioning fluorescence microscopy. *Nano Lett.* **2021**, *21*, 5133−5142.
(30) Abdollahramezani, S.; Hemmatyar, O.; Adibi, A. Meta-optics for spatial optical analog computing. *Nanophotonics* **2020**, *9*, 4075−4095.
(31) Huo, P.; et al. Photonic spin-multiplexing metasurface for switchable spiral phase contrast imaging. *Nano Lett.* **2020**, *20*, 2791−2798.

(32) Wan, L.; Pan, D.; Feng, T.; Liu, W.; Potapov, A. A. A review of dielectric optical metasurfaces for spatial differentiation and edge detection. *Frontiers of Optoelectronics* **2021**, *14*, 187−200.
(33) Kim, Y.; Lee, G. Y.; Sung, J.; Jang, J.; Lee, B. Spiral metalens for phase contrast imaging. *Adv. Funct. Mater.* **2022**, *32*, 2106050.
(34) Xu, D.; et al. Inverse design of Pancharatnam−Berry phase metasurfaces for all-optical image edge detection. *Appl. Phys. Lett.* **2022**, *120*, 241101.
(35) Zhang, Y.; et al. Dielectric Metasurface for Synchronously Spiral Phase Contrast and Bright-Field Imaging. *Nano Lett.* **2023**, *23*, 2991.
(36) Wang, X.; et al. Single-shot isotropic differential interference contrast microscopy. *Nat. Commun.* **2023**, *14*, 2063.
(37) Zhou, J.; et al. Nonlinear computational edge detection metalens. *Adv. Funct. Mater.* **2022**, *32*, 2204734.
(38) Tanriover, I.; Dereshgi, S. A.; Aydin, K. Metasurface enabled broadband all optical edge detection in visible frequencies. *Nat. Commun.* **2023**, *14*, 6484.
(39) Falk, T.; et al. U-Net: deep learning for cell counting, detection, and morphometry. *Nat. Methods* **2019**, *16*, 67−70.
(40) Moen, E.; et al. Deep learning for cellular image analysis. *Nat. Methods* **2019**, *16*, 1233−1246.
(41) von Chamier, L.; et al. Democratising deep learning for microscopy with ZeroCostDL4Mic. *Nat. Commun.* **2021**, *12*, 2276.
(42) Midtvedt, B.; et al. Single-shot self-supervised object detection in microscopy. *Nat. Commun.* **2022**, *13*, 7492.
(43) Sinha, A.; Lee, J.; Li, S.; Barbastathis, G. Lensless computational imaging through deep learning. *Optica* **2017**, *4*, 1117−1125.
(44) Ning, K.; et al. Deep-learning-based whole-brain imaging at single-neuron resolution. *Biomed. Opt. Express* **2020**, *11*, 3567−3584.
(45) Li, A.-C.; et al. Patch-based U-net model for isotropic quantitative differential phase contrast imaging. *IEEE Trans. Med. Imaging* **2021**, *40*, 3229−3237.
(46) Chadebecq, F.; Lovat, L. B.; Stoyanov, D. Artificial intelligence and automation in endoscopy and surgery. *Nat. Rev. Gastroenterol. Hepatol.* **2023**, *20*, 171.
(47) Bian, Y.; et al. Deep learning virtual Zernike phase contrast imaging for singlet microscopy. *AIP Adv.* **2021**, *11*, No. 065311.
(48) Chen, Y.-J.; Vyas, S.; Huang, H.-M.; Luo, Y. Self-supervised neural network for phase retrieval in QDPC microscopy. *Opt. Express* **2023**, *31*, 19897−19908.
(49) Nadell, C. C.; Huang, B.; Malof, J. M.; Padilla, W. J. Deep learning for accelerated all-dielectric metasurface design. *Opt. Express* **2019**, *27*, 27523−27535.
(50) Tseng, E.; et al. Neural nano-optics for high-quality thin lens imaging. *Nat. Commun.* **2021**, *12*, 6493.
(51) Liu, Z.; Zhu, D.; Rodrigues, S. P.; Lee, K.-T.; Cai, W. Generative model for the inverse design of metasurfaces. *Nano Lett.* **2018**, *18*, 6570−6576.
(52) Chen, M. K.; Liu, X.; Sun, Y.; Tsai, D. P. Artificial intelligence in meta-optics. *Chem. Rev.* **2022**, *122*, 15356−15413.
(53) Wang, F.; Zhao, S.; Wen, Y.; Sun, J.; Zhou, J. High Efficiency Visible Achromatic Metalens Design via Deep Learning. *Adv. Opt. Mater.* **2023**, *11*, 2300394.
(54) Chen, M. K.; et al. A meta-device for intelligent depth perception. *Adv. Mater.* **2023**, *35*, 2107465.
(55) An, S.; et al. A deep learning approach for objective-driven all-dielectric metasurface design. *ACS Photonics* **2019**, *6*, 3196−3207.
(56) Wang, S.; et al. A broadband achromatic metalens in the visible. *Nat. Nanotechnol.* **2018**, *13*, 227−232.
(57) Kawashima, T.; Yoshikawa, H.; Adachi, S.; Fuke, S.; Ohtsuka, K. Optical properties of hexagonal GaN. *J. Appl. Phys.* **1997**, *82*, 3528−3535.
(58) Wang, J.; Perez, L. The effectiveness of data augmentation in image classification using deep learning. *arXiv* **2017**, DOI: 10.48550/arXiv.1712.04621.
(59) Larose, D. T.; Larose, C. D. *Discovering knowledge in data: an introduction to data mining*; John Wiley & Sons, 2014; Vol. *4*.
(60) Moriasi, D. N.; et al. Model evaluation guidelines for systematic quantification of accuracy in watershed simulations. *Trans. ASABE* **2007**, *50*, 885−900.
(61) Kingma, D. P.; Ba, J. Adam: A method for stochastic optimization. *arXiv* **2014**, DOI: 10.48550/arXiv.1412.6980.

https://doi.org/10.1021/acs.nanolett.3c03484
Nano Lett. 2023, 23, 11630−11637

Intelligent Phase Contrast Meta-Microscope System

Cheng Hung Chu[1], Yu-Hsin Chia[2,3], Hung-Chuan Hsu[4], Sunil Vyas[2], Chen-Ming Tsai[2], Takeshi Yamaguchi[5], Takuo Tanaka[5], Huei-Wen Chen[6,7], Yuan Luo[1,2,3,8*], Pan-Chyr Yang[1,8,9,10*], and Din Ping Tsai[11,12,13*]

[1]YongLin Institute of Health, National Taiwan University, Taipei 10672, Taiwan
[2]Institute of Medical Device and Imaging, National Taiwan University, Taipei 10051, Taiwan
[3]Institute of Biomedical Engineering, National Taiwan University, Taipei 10051, Taiwan
[4]Department of Mechanical Engineering, National Taiwan University, Taipei 10617, Taiwan
[5]Innovative Photon Manipulation Research Team, RIKEN Center for Advanced Photonics, Saitama 351-0198, Japan
[6]Graduate Institute of Toxicology, College of Medicine, National Taiwan University, Taipei 100, Taiwan
[7]Genome and Systems Biology Degree Program, National Taiwan University and Academia Sinica, Taipei 100, Taiwan.
[8]Program for Precision Health and Intelligent Medicine, National Taiwan University, Taipei, 106319, Taiwan, R.O.C.
[9]Department of Internal Medicine, National Taiwan University Hospital, National Taiwan University, Taipei 10002, Taiwan
[10]Institute of Biomedical Sciences, Academia Sinica, Taipei 11529, Taiwan
[11]Department of Electrical Engineering, City University of Hong Kong, Kowloon 999077, Hong Kong
[12]Centre for Biosystems, Neuroscience, and Nanotechnology, City University of Hong Kong, Kowloon 999077, Hong Kong
[13]The State Key Laboratory of Terahertz and Millimeter Waves, City University of Hong Kong, Kowloon 99907, Hong Kong

*Corresponding authors: yuanluo@ntu.edu.tw, pcyang@ntu.edu.tw, dptsai@cityu.edu.hk

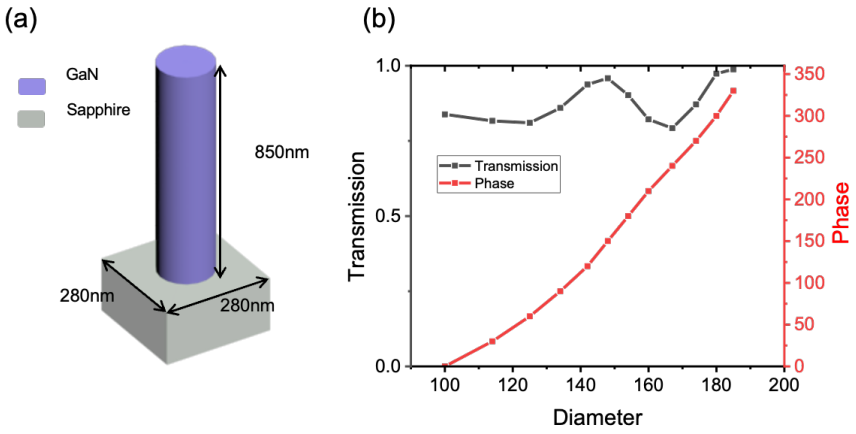

Figure S1. (a) Schematic of GaN nanopillar with a height of 850 nm on a sapphire substrate arranged in a square lattice with a period of 280 nm as a building block. (b) Transmittance and phase shift of the GaN nanopillars with various diameters at wavelength λ = 532 nm used to construct the metalens and metasurface.

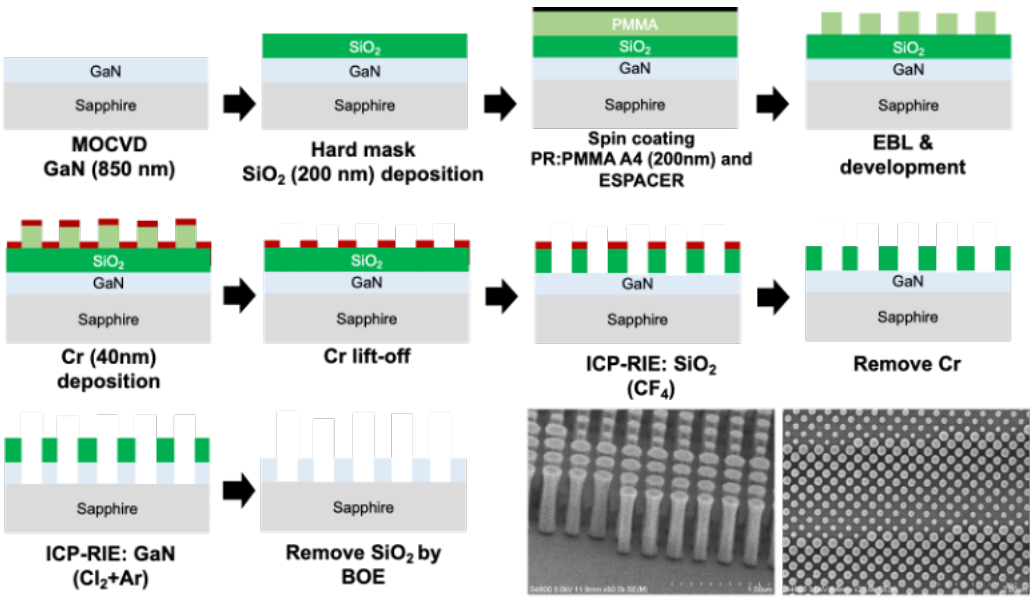

Figure S2. Fabrication procedure of GaN nanopillars and the scanning electron microscope (SEM) image of fabricated metalens [1, 2].

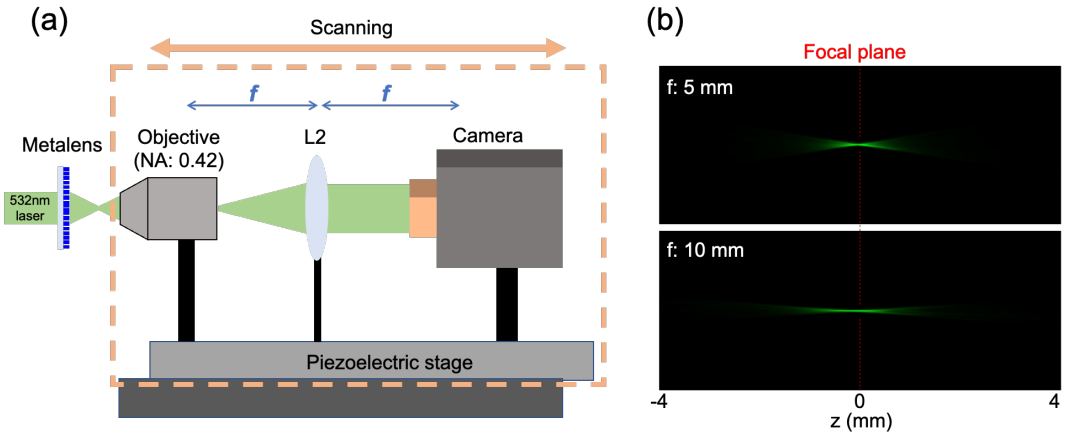

Figure S3. (a) Experimental setup for beam profile measurement (b) Measured intensity distribution for propagation trajectory of the metalens in free space.

The optical characterization setup is shown in Figure S3(a). Laser light with a wavelength of 532 nm and linear polarization is incident from the substrate side of the metalens (Cobalt SambaTM 1500). The motorized stage holding the objective lens (Mitutoyo, BD Plan Apo 20× magnification, NA = 0.28) and CCD (Canon, EOS 650D) moves along the optical axis with the step of 40 μm to record the intensity distribution at different focal planes. Figure S3(b) shows the measured intensity profiles along the propagation direction of two metalenses (± 4 mm focal plane). The average focusing efficiency of metalenses is about 40% at a wavelength of 532 nm.

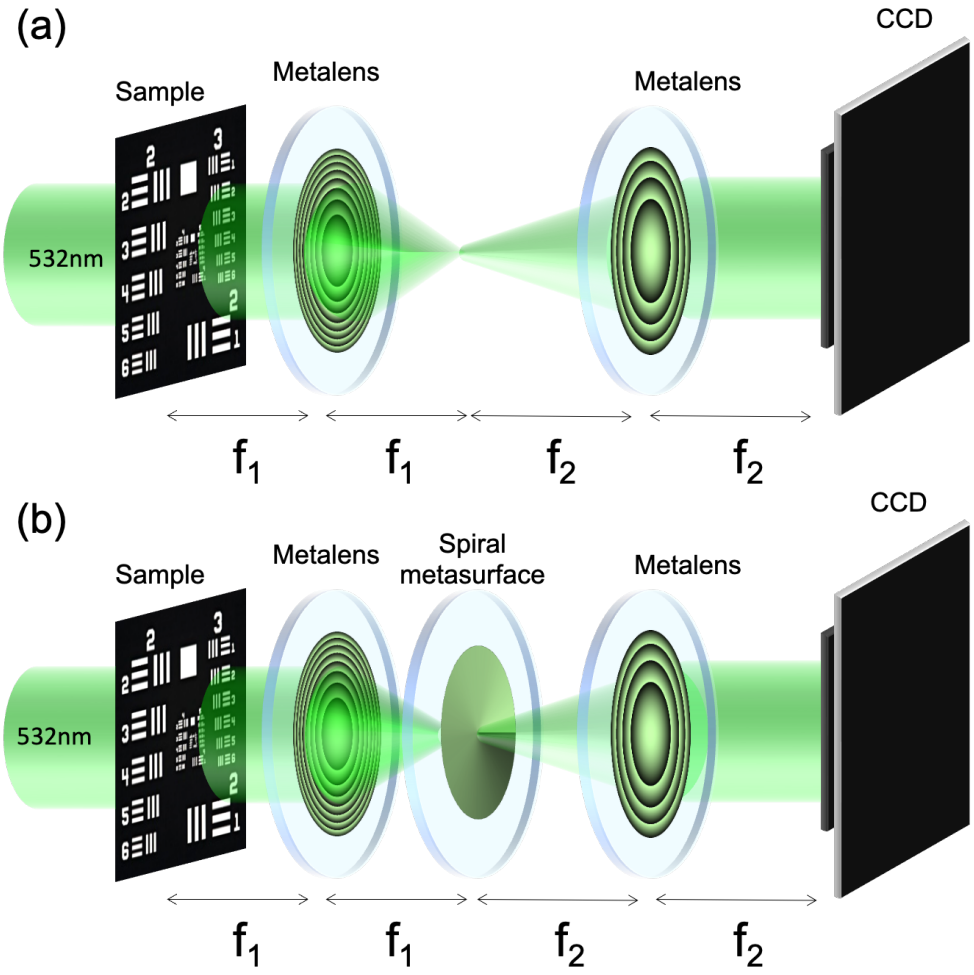

Figure S4. (a) Meta-microscope setup for bright field imaging (b) Meta-microscope setup with spiral metasurface for phase contrast imaging.

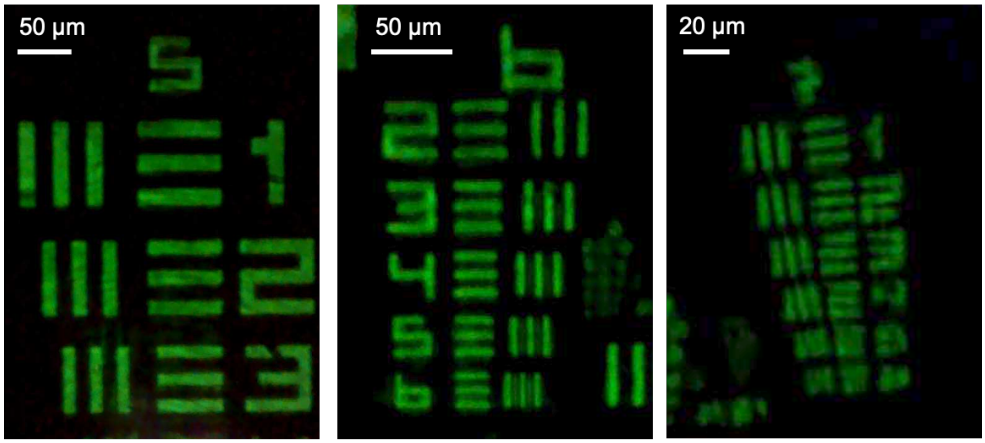

Figure S5. Bright-field image of 1951 resolution test target from group 5 to group 7 obtained from meta-microscope.

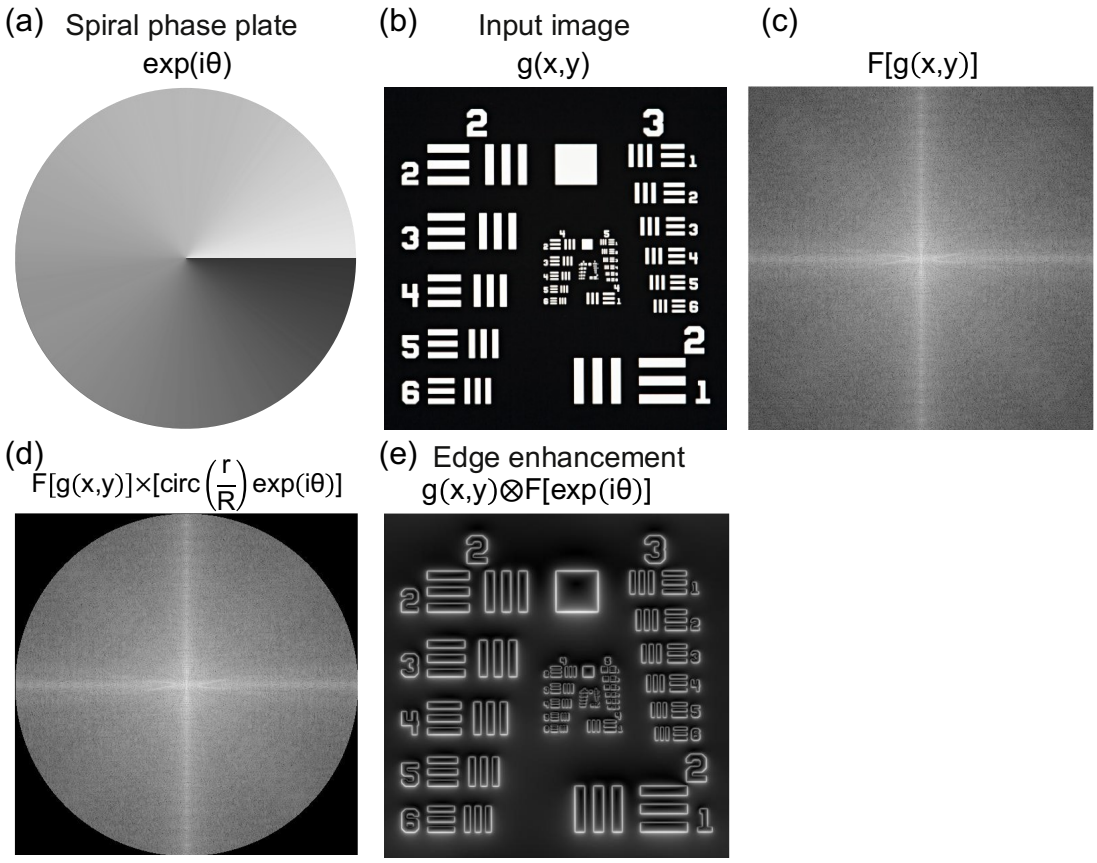

Figure S6. (a) Spiral phase distribution (b) Resolution target as the input image (c) Fourier transform of the input image in the spatial frequency domain (d) Input image convolute with spiral phase plate in the spatial frequency domain (e) Edge-enhanced image obtained by the Fourier transform of (d).

The phase distribution of the spiral (helical) phase plate with a topological charge of 1, $\varphi(r,\theta)=\exp(i\theta)$, is shown in Figure S6(a), where r and θ are the radial distance and azimuthal angle. The input function of the 1951 resolution test chart in the real space g(x,y) is shown in Figure S6(b). The Fourier transform of the input function is shown in Figure S6(c). The Fourier transform of g(x,y) is multiplied by the cir(r/R)exp(iθ), the radial Hilbert transform function, in the frequency domain. The output image represents the convolution between the input image and the radial Hilbert transform function: $I = g(x,y) * h(r,\theta)$.

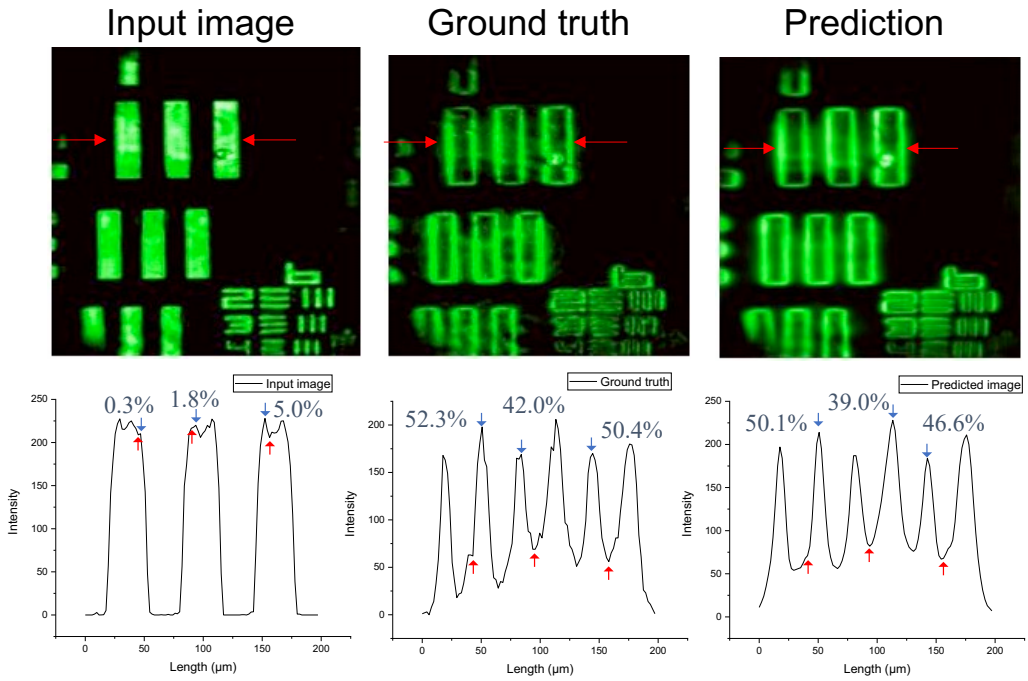

Figure S7. Bright-field image (input), edge-enhanced image (ground truth), and DL-based edge-enhanced image (prediction) of group 4 element 1 of the resolution chart.

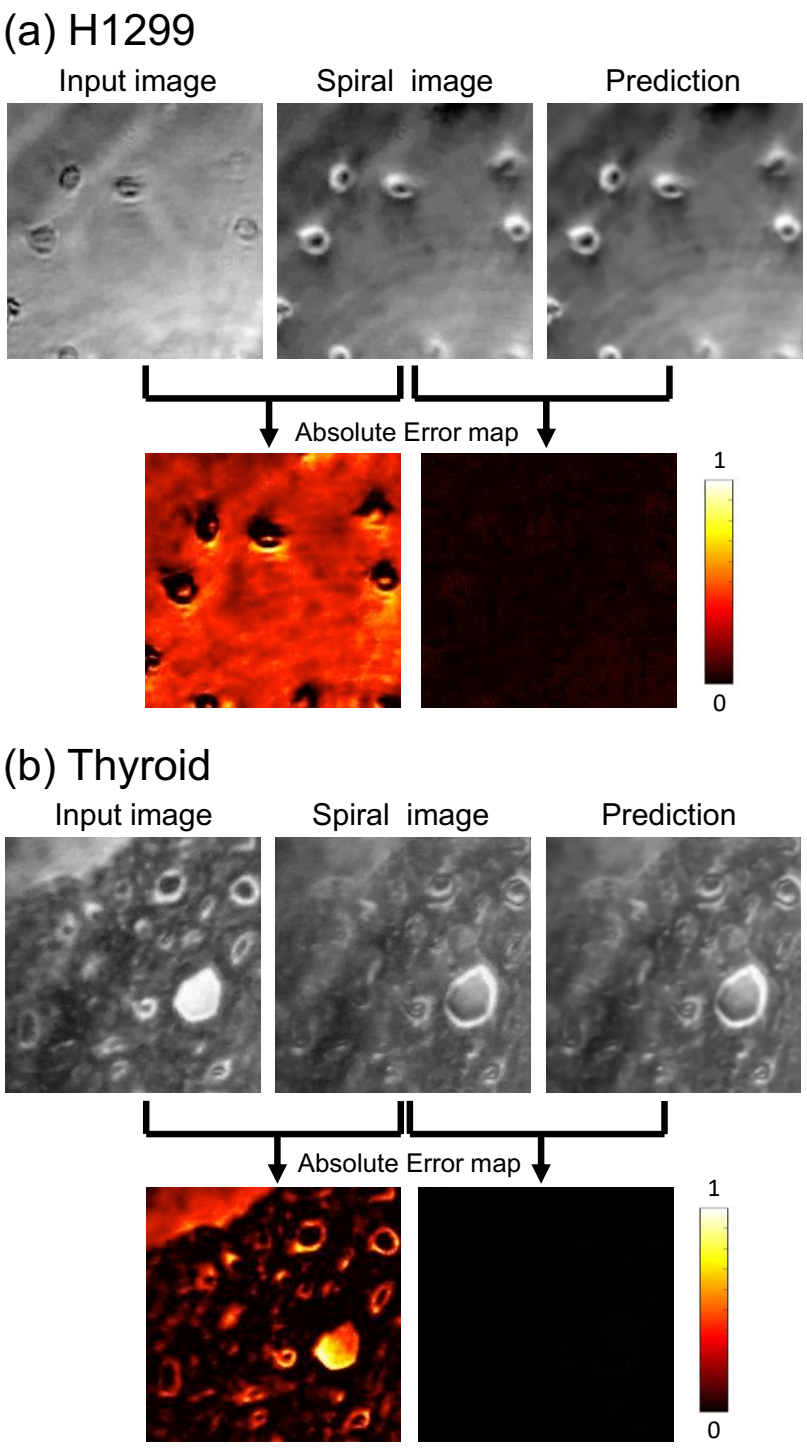

Figure S8. Bright-field image (input), edge-enhanced image (ground truth), and DL-based edge-enhanced image (prediction) of H1299 and Thyroid. The absolute error map on the left shows the difference between the input image and the ground truth, and the error map on the right shows the difference between the ground truth and the prediction generated by our ResNet model.

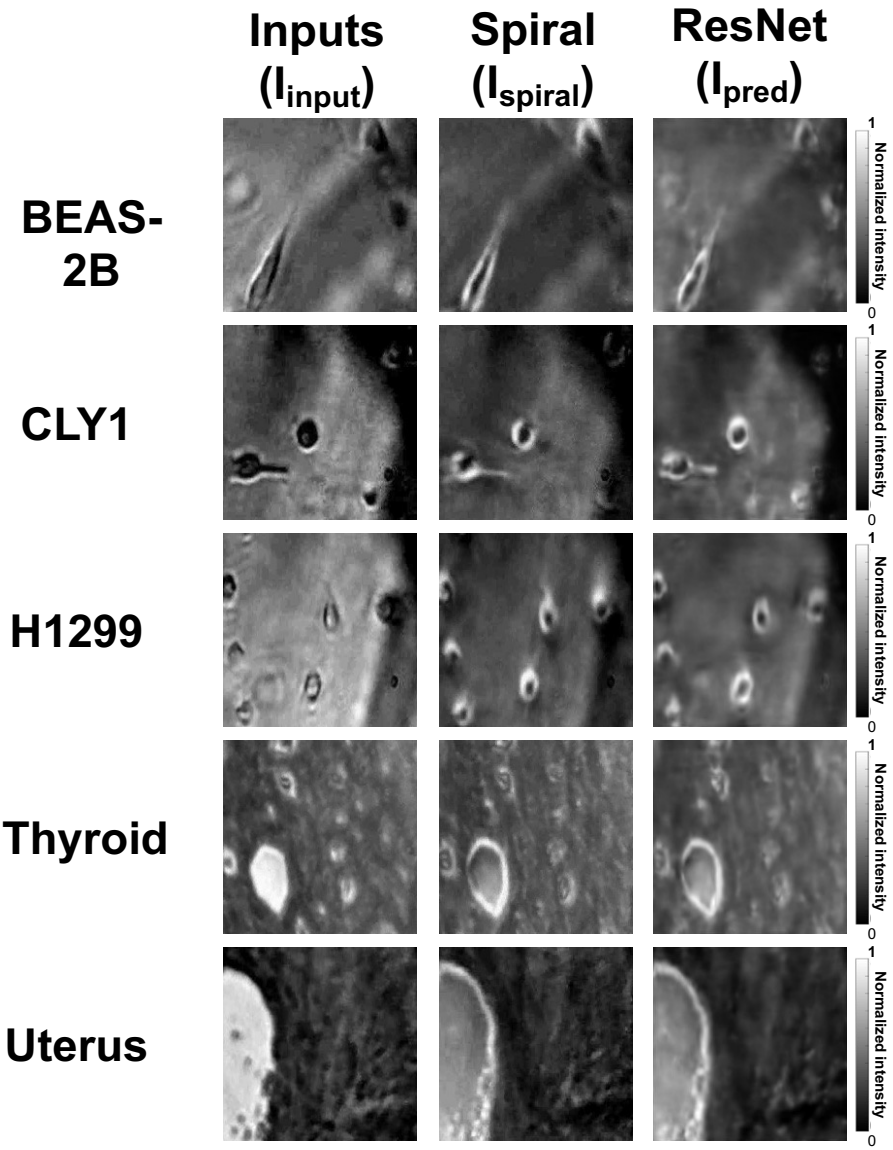

Figure S9. Different types of cells for deep learning model training

Table S1. The encoder architecture of the ResNet model

Input	Output	Output shape	Type
Inputs	Inputs	(200,200,1)	Input image
Inputs	Conv1_1	(200,200,64)	Conv2D 3x3
Conv1_1	Conv1_2	(200,200,64)	Conv2D 3x3
Inputs	Conv1_3	(200,200,64)	Conv2D 1x1
Conv1_2, Conv1_3	Skip1	(200,200,64)	Add
Skip1	Conv2_1	(100,100,128)	Conv2D 3x3 Stride = 2
Conv2_1	Conv2_2	(100,100,128)	Conv2D 3x3
Skip1	Conv2_3	(100,100,128)	Conv2D 1x1 Stride = 2
Conv2_2, Conv2_3	Skip2	(100,100,128)	Add
Skip2	Conv3_1	(50,50,256)	Conv2D 3x3 Stride = 2
Conv3_1	Conv3_2	(50,50,256)	Conv2D 3x3
Skip2	Conv3_3	(50,50,256)	Conv2D 1x1 Stride = 2
Conv3_2, Conv3_3	Skip3	(50,50,256)	Add
Skip3	Conv4_1	(25,25,512)	Conv2D 3x3 Stride = 2
Conv4_1	Conv4_2	(25,25,512)	Conv2D 3x3
Skip3	Conv4_3	(25,25,512)	Conv2D 1x1 Stride = 2
Conv4_2, Conv4_3	Skip4	(25,25,512)	Add

Table S2. The decoder architecture of the ResNet model

Input	Output	Output shape	Type
Skip4	Up1_1	(50,50,512)	UpSampling2D
Up1_1, Skip3	Sum_1	(50, 50, 768)	Concatenate
Sum_1	Conv5_1	(50,50,256)	Conv2D 3x3
Conv5_1	Conv5_2	(50,50,256)	Conv2D 3x3
Sum_1	Conv5_3	(50,50,256)	Conv2D 1x1
Conv5_2, Conv5_3	d1	(50,50,256)	Add
d1	Up2_1	(100,100,256)	UpSampling2D
Up2_1, Skip2	Sum_2	(100,100,384)	Concatenate
Sum_2	Conv6_1	(100,100,128)	Conv2D 3x3
Conv6_1	Conv6_2	(100,100,128)	Conv2D 3x3
Sum_2	Conv6_3	(100,100,128)	Conv2D 1x1
Conv6_2, Conv6_3	d2	(100,100,128)	Add
d2	Up3_1	(200,200,128)	UpSampling2D
Up3_1, Skip1	Sum_3	(200,200,192)	Concatenate
Sum_3	Conv7_1	(200,200,64)	Conv2D 3x3
Conv7_1	Conv7_2	(200,200,64)	Conv2D 3x3
Sum_3	Conv7_3	(200,200,64)	Conv2D 1x1
Conv7_2, Conv7_3	d3	(200,200,64)	Add
d3	Output	(200,200,1)	Conv2D 1x1

References

1. Wang, S.M.; Wu, P.C.; Su, V.C.; Lai, Y.C.; Chen, M.K.; Kuo, H.Y.; Chen, B.H.; Chen, Y.H.; Huang, T.T.; Wang, J.H; et al. A broadband achromatic metalens in the visible. Nat. Nanotechnol. 2018, 13, 227–232.

2. Kawashima, T.; Yoshikawa, H.; Adachi, S.; Fuke, S.; Ohtsuka, K. Optical properties of hexagonal gan. J. Appl. Phys. 1997, 82, 3528–3535.